Pantograph Arc Location Estimation Using Resonant Frequencies in DC Railway Power Systems

Fulin Fan, Andreas Wank, Yljon Seferi, *Graduate Student Member, IEEE*, and Brian G. Stewart, *Member, IEEE*

***Abstract*— Pantograph arcing in electrified railway systems not only reduces the power collection quality of a locomotive but can also damage pantograph strips and overhead lines (OHLs). Most research detects pantograph-to-OHL arcs based on onboard voltage/current measurements, pantograph cameras, and so on. The use of onboard voltage/current data, though being cost-effective, rarely reflects arc locations along OHLs. This article develops an arc positioning method, which matches the position-dependent resonant frequency (RF) of an OHL with the RF extracted from voltage measurements in a pantograph arc event. A particular 20-km DC railway line supplied by two substations is first modelled in MATLAB/Simulink, with the model effectiveness being assessed based on voltage measurements in an arc event. Then, the OHL-related RFs estimated by the model are validated by the Tableau formula and discussed alongside impacts on RFs based on line models, locomotive locations, and line lengths. These evaluations permit the generation of an RF curve that links OHL-related RFs with arc locations. The arc positioning method is tested based on the pantograph arc events presumed at various positions along the 20-km line, showing errors within 0.2 km at certain locations. The ability to determine arc locations will permit periodic inspections to be performed on the determined line sections.**

***Index Terms*— DC traction power supply system, overhead line (OHL), pantograph arc location estimation, resonant frequency (RF).**

I. Introduction

THE electrification of rail transport has played a major role in decarbonization through increased energy efficiency and reduced reliance on fossil fuels [1]–[3]. In a DC railway power system, the electrical power of upstream AC grids is rectified into DC power at traction substations (TSSs) and then transferred to an electrical locomotive via an overhead line (OHL) suspended along the track or an electrical third rail mounted at the track level; the locomotive collects the power through its pantograph (or contact shoe), which contacts with the OHL (or third rail) [4], [5]. Therefore, the power collection of a locomotive is significantly affected by the quality of the sliding contact between the pantograph and the OHL.

The increasing speed of trains makes it difficult to maintain a regular pantograph-to-OHL contact due to the enlarged impact of dynamic components on contact force [6]. Contact force falling below a certain level will cause a contact loss, leading to an undesired pantograph arc, especially when a heavy current passes through the point of contact [7], [8]. The energy dissipated in the pantograph arc not only decreases the energy efficiency of the railway system but may also result in electrical erosion and fusion for both the pantograph and the OHL, accelerating any deterioration [9] and, in turn, causing more arcs. This will progressively degrade the quality of pantograph-to-OHL sliding contact and power collection and may even lead to failure of the overhead contact system [7].

A minimum pantograph-to-OHL contact force is normally required in practice to avoid pantograph arc occurrences caused by OHL irregularity [10], [11] and wear [12]. The contact force is generally monitored at a frequency limited to 20 Hz though the arc duration can reach 5 ms (i.e., equivalent to 200 Hz) [13] such that high-frequency contact losses cannot be completely reflected by measurements. The pantograph-OHL interaction performance at high frequencies has been investigated in [14] to capture high-frequency contact losses that associate with pantograph arcing so as to maintain the dynamic performance of sliding contact as required [15]. Some research has also been devoted to developing methods for arc detection, which supplies a basis for predictive maintenance, providing a cost-effective solution to maintenance schedules [16]. By means of a camera installed on the roof of a train, a recorded pantograph video can be analysed by signal and image processing methods to detect the pantograph arc occurrence [16]–[19]. For example, continuous frame-by-frame images decomposed from a pantograph video could be converted into binary images from which the ratio of white pixels to black pixels is evaluated as an arc parameter for the frame [17]. In addition, some arc detection techniques install sensors to monitor physical quantities emitted from pantograph arcing, such as: 1) significant temperature changes at the contact point recorded by thermal cameras combined with image processing algorithms [20]; 2) ultraviolet emissions detected by phototubes [7], [21] or predefined

Manuscript received December 2, 2020; revised February 16, 2021; accepted February 18, 2021. Date of publication February 24, 2021; date of current version October 1, 2021. This work was supported in part by the EMPIR Programme co-financed by the Participating States and in part by the European Union's Horizon 2020 Research and Innovation Programme. *(Corresponding author: Fulin Fan.)*

Fulin Fan, Yljon Seferi, and Brian G. Stewart are with the Institute for Energy and Environment, University of Strathclyde, Glasgow G1 1XW, U.K. (e-mail: f.fan@strath.ac.uk; yljon.seferi@strath.ac.uk; brian.stewart.100@strath.ac.uk).

Andreas Wank is with the National Physical Laboratory, Glasgow G1 1RD, U.K. (e-mail: andreas.wank@npl.co.uk).

Digital Object Identifier 10.1109/TTE.2021.3062229

light wavelengths for particular metal materials monitored by light detectors [22]; and 3) the electromagnetic field radiation captured by an antenna [23], [24] and processed to determine the possible characteristic radiated frequencies [23]. However, these approaches, which are suitable for the one-time diagnostic, require relevant monitoring devices. In order to avoid investment in additional sensors, some algorithms have been developed to extract useful arcing information from measurements of pantograph voltage and current (V–I) that are already available onboard trains and can be implemented for daily monitoring by operating trains. Traction current data were decomposed in [25] by using wavelet multiresolution analysis from which the arc occurrence was estimated. The low-frequency oscillation characteristics of pantograph current associated with arcing in DC railway systems were exploited in [26]. In [27] and [28], support vector machine learning models were trained based on the V–I data combined with the presence or absence of arc events detected by phototubes and then applied to V–I measurements to isolate healthy and arc occurring conditions, correctly identifying about 80% of the events. Without the phototube signal-based training, an unsupervised classification technique was applied in [29] to separate pantograph current measurements into different clusters, which indicated the presence and the average magnitude of an arc event.

The V–I-based methods proposed in [25]–[29] have shown the capability of arc detection. However, they are unable to determine the location of an arc event, unless the time synchronisation of the arc event and the position of the locomotive are both known. This is important to determine the line section requiring inspections and, thus, prevent extended interruptions of transportation services due to the inspection of a complete line. To assist in locating the position of arc events, this article proposes an enhancement of V–I-based methods to capture the arc location from information embedded in the voltage waveforms based on the fact that the train movement changes the network topology and, thus, the resonant frequency (RF) related to the line. The arc positioning method proposes that the location is achieved by matching the OHL-related RF determined for different locomotive positions with the RF estimated from the voltage measurements during a measured pantograph arc event.

This article first models in MATLAB/Simulink a 3-kV DC traction power supply system supplied by two TSSs. The measured distortion of the voltage waveform incurred by an arc event is then replicated in order to assess the model effectiveness. Then, the RFs related to the OHL split at different locomotive positions are determined by the use of the Simulink model and validated by the modified Tableau formula where the line is modelled by a finite number of cascaded π-sections with lumped parameters. The OHL-related RFs simulated by different numbers of π-sections and a distributed parameter line (DPL) model are compared to illustrate the necessity of modelling the line with distributed parameters for a more accurate response. Based on the DPL model, the RFs related to the line are estimated for varying locomotive locations. This evaluation creates an RF curve linking the OHL-related RF with the arc position. The RF curve is then tentatively

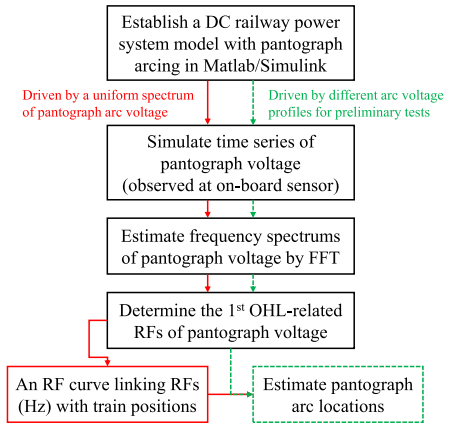

Fig. 1. Process of the RF-based pantograph arc location estimation method and preliminary tests.

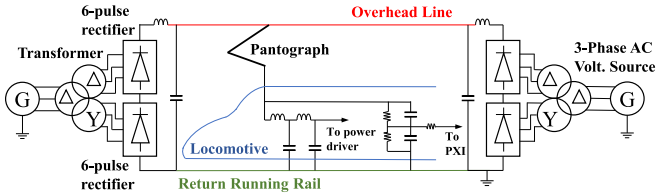

Fig. 2. Scheme of the locomotive in the DC traction power supply system.

employed to estimate the presumed arc event positions along a 20-km line. A flowchart describing the process of the proposed arc positioning method and its preliminary tests is shown in Fig. 1. The pantograph arc location estimation method proposed here, starting from the perspective of RFs in DC railway power systems, exploits the relationship of the OHL-related RF with the locomotive position along an OHL. It could provide a new idea for determining pantograph arc locations and line sections requiring inspections based only on the onboard V–I data and encourage the development of onboard monitoring devices that permit capturing the OHL-related RFs from V–I measurements.

This article is structured as follows. Section II describes the modelling of the 3-kV DC railway traction power supply system by MATLAB/Simulink and Tableau formula. Section III compares the OHL-related RFs estimated by different approaches and line models. Section IV generates the RF curve for the arc location estimation and preliminarily tests the arc positioning method. Section V discusses the potential application of the proposed method with respect to double-pantograph modes, requirements on monitoring devices and data processing, and line impedance uncertainties. Conclusions and recommendations for further work are presented in Section VI.

II. Modelling of DC Traction Power Supply System

A. DC Traction Power Supply System Model in Simulink

This work studies the 3-kV DC traction power supply system supporting a single-track railway line between Pisa

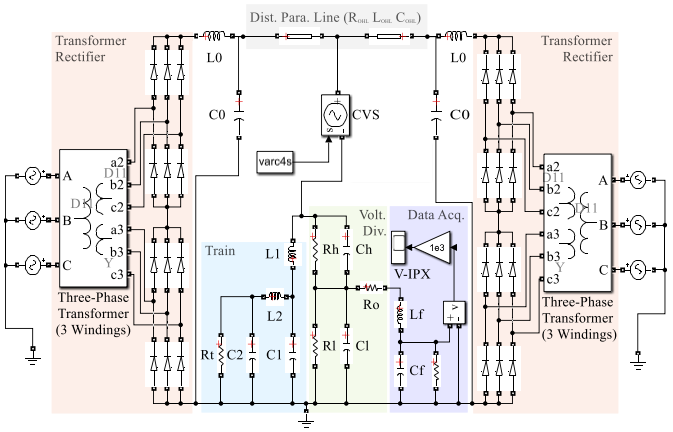

Fig. 3. Simulation model of the Pisa–Collesalvetti line with the locomotive.

TABLE I
VALUES OF KEY CIRCUITAL COMPONENTS [30]

L0	6 mH	L1	45 mH	Rh	6 MΩ	Ro	50 Ω
C0	350 μF	C1	5 mF	Rl	5.9 kΩ	R_{OHL}	0.17 Ω/km
Lf	20 mH	L2	507 μH	Ch	790 pF	L_{OHL}	0.57 mH/km
Cf	116 nF	C2	4 mF	Cl	787 nF	C_{OHL}	20 nF/km

and Collesalvetti in Italy (see Fig. 2) [30]. The railway line is fed by two TSSs separated by 20 km. Each TSSs consists of a rectifier to convert the AC grid voltage into 3.7-kV DC and an *LC* second-order low-pass filter, which is connected at the TSS output to smooth the voltage ripple. The traction system of the train ETR600 is configured to cascade two *LC* low-pass filters at the input stage [30], which attenuates the ripple in the collected current and mitigates harmonic emissions and incoming disturbances. The pantograph V–I is monitored by a calibrated resistive–capacitive voltage divider, with the output signals being sent to a National Instrument PXI module through an analog/digital/analog optical link and a data acquisition module with a sampling rate of 50 kHz [30].

Fig. 3 shows the simulation model of the Pisa–Collesalvetti DC railway power system developed in MATLAB/Simulink [31]. The TSS is modelled by a combination of a three-phase AC voltage source and a transformer rectifier [32], followed by an *LC* low-pass filter. Each segment of the 20-km OHL split by the locomotive is modelled by a DPL [33]. A controlled voltage source (CVS) is placed between the OHL and the train input to simulate the profile of the pantograph arc voltage V_{arc}, which will be adjusted to replicate field measurements of the pantograph voltage V_p, while the arc resistance in the order of 10–100 mΩ [34] being small compared to the overall OHL impedance [35] is generally negligible in the system simulation [30], [35]. The data acquisition system (DAS) following the voltage divider is simulated by an *LC* low-pass filter with an RF of about 3.3 kHz [30]. The train is modelled as a constant resistor Rt = 2.37 Ω. The values of circuital components are tabulated in Table I.

The field measurements of V_p over a particular 4-s period [30] provided by Trenitalia are plotted in Fig. 4 where a significant disturbance was caused by a pantograph arc event

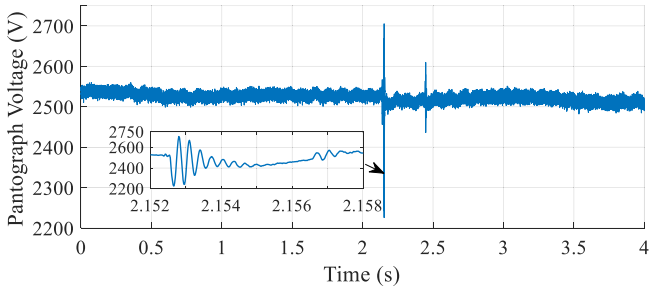

Fig. 4. Measurements of pantograph voltage during a particular 4-s interval.

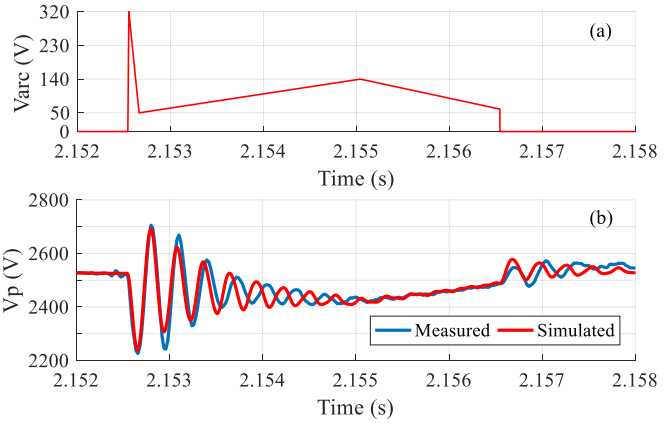

Fig. 5. (a) Fine-tuned profile of pantograph arc voltage V_{arc} and (b) resulting simulation of pantograph voltage V_p against the measured V_p.

which lasted about 4 ms from 2.1525 to 2.1565 s. In order to replicate the V_p measurements, different V_{arc} shapes derived from the V_{arc} profile optimised in [30] (i.e., [30, Fig. 16]) have been tested to improve the consistency between the simulated and measured V_p. Fig. 5 shows a fine-tuned profile of V_{arc} and the resulting V_p waveform when the locomotive is positioned at the middle of the line. The disturbance of V_p is shown to follow the V_{arc} shape, with oscillations after the ignition and extinction of pantograph arcing. These significant oscillations are found to be mainly associated with the *LC* components at the TSS output, which have RFs of around 110 Hz through an examination of the V_p waveforms after removing different components within the circuit. Although the simplification of the actual V_{arc} profile and the residual electrical elements in the network contribute to the difficulty of completely replicating the field measurements of V_p, the simulated V_p is reasonably matched with the measured arc event signal and illustrates the effectiveness of the railway power system model.

B. Simplified Simulink Model for RF Estimation

Given that the modelling focuses on the transient event where V_{arc} is the only applied voltage, the complete Simulink model in Fig. 3 is simplified by replacing each TSS with a resistor R0 = 0.1 Ω that represents the internal resistance of the TSS. Hence, the only voltage source left in the model is the CVS. It has been examined that the complete and simplified models produce almost the same distortion of V_p with a slight periodic difference of around 600 Hz (i.e., equivalent

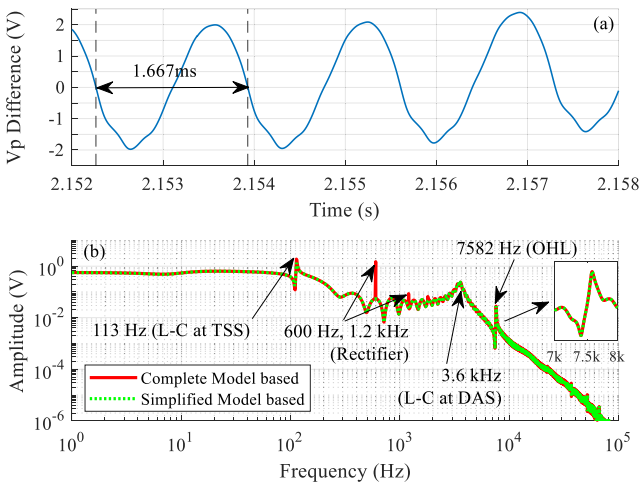

Fig. 6. (a) Differences (V) between pantograph voltage V_p waveforms simulated by the complete and simplified models in an arc event and (b) their respective frequency spectrums.

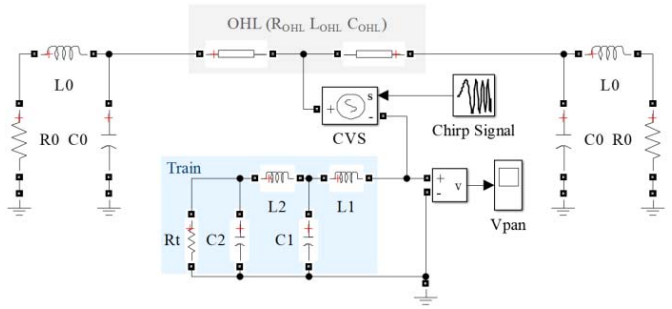

Fig. 7. Simplified model of the Pisa–Collesalvetti line with the locomotive.

to 1.667 ms), as shown in Fig. 6(a). This is because the simplified model cannot reflect the harmonics caused by the 12-pulse rectifiers (i.e., integer multiples of the 12th harmonics of 50 Hz) though it generates the same OHL-related RFs as the complete model, as shown in Fig. 6(b). The relatively higher amplitudes of resonances associated with the *LC* filters at the TSS output in Fig. 6(b) can also explain the significant oscillations of V_p in Fig. 5(b).

In order to obtain more general results and avoid the impact that the V–I monitoring device has on the RFs, the voltage divider and the DAS are additionally removed, with the voltage at the input stage of the train being monitored directly, as shown in Fig. 7. The values of circuital components in the simplified model in Fig. 7 are equal to those with the same symbols in the complete model in Fig. 3. A chirp signal [36], which generates a sine wave with frequency linearly increasing from 0 to 500 kHz in 2 s, is used as the input signal of the CVS in the simplified model (see Fig. 7). Then, the fast Fourier transform [37] is applied to the simulated V_p and the chirp signal, respectively, to form their spectrums. Since the frequency component (FC) of the chirp signal fluctuating at lower and higher frequency levels (see Fig. 8) may be misleading with regard to the RF estimation (especially at the lower end), the spectrum of V_p is calibrated by dividing its FCs

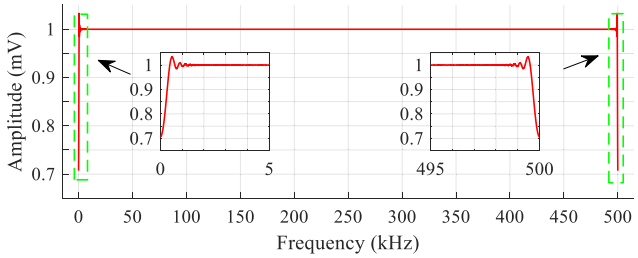

Fig. 8. Frequency spectrum of the chirp signal.

by the corresponding FCs of the chirp signal. The calibrated V_p spectrum can be regarded as that obtained when the CVS input signal has a uniform frequency spectrum and will be used to estimate the RFs related to the OHL, i.e., the locations of the peaks in the spectrum beyond 1 kHz. The process of determining the OHL-related RFs ($\mathrm{RF_{OHL}}$) is formulated by the following equation:

$$\mathrm{RF_{OHL}} = \mathrm{findpeaks}\left(\frac{\mathrm{FFT}(V_p)}{\mathrm{FFT}(V_{\mathrm{ch}})}; \geq 1\ \mathrm{kHz}\right) \tag{1}$$

where $\mathrm{FFT}(\cdot)$ is the fast Fourier transform that determines the spectrums of V_p and the chirp signal V_{ch}; the operator findpeaks$(\cdot; \geq 1$ kHz) represents the operation that detects the peak locations in the calibrated spectrum beyond 1 kHz.

C. Distributed and Lumped Parameter Line Models

A DPL model assumes that the resistance, inductance, and capacitance are uniformly distributed along an OHL [38] where the shunt conductance is usually neglected due to a considerably small leakage current [39]. The OHL segment on the left- or right-hand side of the pantograph can be simulated by a single DPL in the Simulink models in Figs. 3 and 7. However, the DPL model having an infinite number of states is not suitable for the state-space representation [40]. To validate the Simulink model-based RFs by the Tableau formula [41] that requires a finite number of states, the OHL segment on each side of the pantograph can be approximated by a lumped parameter line (LPL) model that cascades a number of identical π-sections [42]. There are finite states in the LPL model, enabling the state-space representation at the cost of a decreased accuracy in the transient response simulation. The maximum frequency range $f_{\max}$ simulated by K π-sections can be approximated by [40]

$$f_{\max} = (K \times v)/(8 \times l_{\mathrm{OHL}}) \tag{2}$$

where v and l_{OHL} denote the propagation speed (km/s) and the length (km) of the line. The approximation of the OHL can be improved by using more π-sections, which, in turn, increases the network complexity and computational burden. This results in a tradeoff in the selection of the number of π-sections between the model complexity and the frequency range of interest.

Fig. 9(a) shows a simplified railway system model with each OHL segment being simulated by two cascaded π-sections. The capacitor at the end of a π-section is parallel connected with the capacitor of its neighboring π-section or

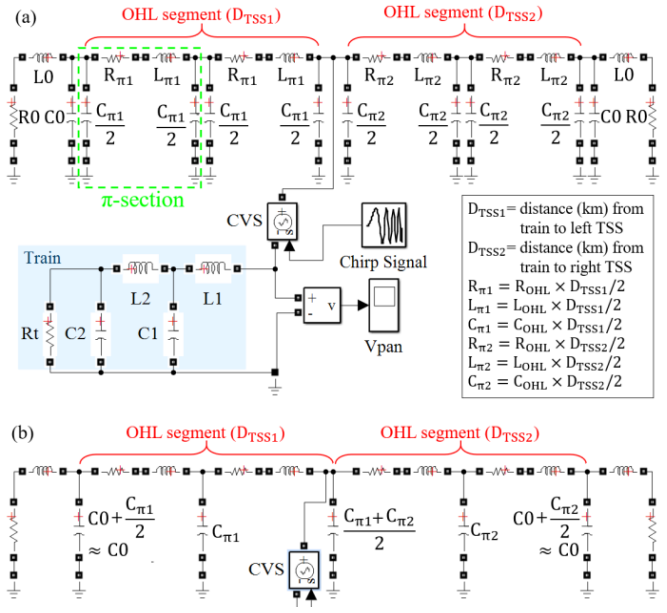

Fig. 9. (a) Simplified DC railway power system model with each OHL segment being modelled by two π-sections and (b) OHL circuit simplified by merging the parallel-connected capacitors.

the capacitor (C0) in the low-pass filter at the output stage of the TSS. The parallel-connected capacitors can then be regarded as a single equivalent capacitor having the sum of the individual capacitances, which will further simplify the representation of the OHL system, as shown in Fig. 9(b). It is noted that the capacitor of a π-section parallel connected with C0 is considerably smaller and negligible compared with C0. Therefore, only three equivalent capacitors remain in the OHL circuit in Fig. 9(b). When modelling each OHL segment by $K\pi$-sections, the number of equivalent capacitors in the OHL circuit will be $(2K-1)$. The number of π-sections used and the locomotive position that determines the length of each OHL segment will affect the network topology and the values of circuital components and, thus, the RFs related to the OHL.

D. Modified Tableau Formulation

The LPL-based simplified railway power system model that has finite states can be expressed by the Tableau formula, which determines the topology of the network by Kirchhoff's current and voltage laws (KCL and KVL) and describes the physics of circuital components by constitutive equations [41]

$$\begin{bmatrix} A & 0 & 0 \\ 0 & 1 & -A^T \\ Z & Y & 0 \end{bmatrix} \cdot \begin{bmatrix} I \\ U \\ V \end{bmatrix} = \begin{bmatrix} 0 \\ 0 \\ W \end{bmatrix} \tag{3}$$

where Z and Y are matrices of impedance and admittance; I, U, and V denote vectors of branch currents, branch voltages, and nodal voltages; the nodal incidence matrix and its transpose are denoted by A and A^T, respectively; and the term W is the vector of independent sources. The matrix of branch voltages U can be eliminated by substituting $U = A^T V$ into $ZI + YU = W$, giving a modified Tableau formula [43]

$$\begin{bmatrix} YA^T & Z \\ 0 & A \end{bmatrix} \cdot \begin{bmatrix} V \\ I \end{bmatrix} = \begin{bmatrix} W \\ 0 \end{bmatrix}. \tag{4}$$

The independent source W that represents the CVS, i.e., the only voltage source in the simplified model (see Fig. 9), is set to 1 V. Then, the voltage at the input stage of the locomotive [i.e., the right node of the L1 branch in Fig. 9(a)] is estimated based on (4), where Z and Y are computed for a particular frequency varying from 0 to 500 kHz. This forms the spectrum of V_p from which the OHL-related RFs are determined. Equation (5) presents an example of the modified Tableau formula for the simplified network of Fig. 9(b). For simplicity, each OHL segment is represented by one π-section, $\mathrm{R0} = \mathrm{R}_{\pi1} = \mathrm{R}_{\pi2} = 0$ and $\mathrm{L1} = \mathrm{L2} = \mathrm{C1} = \mathrm{C2} = 0$. This reduces the 39×39 matrix of the simplified network of Fig. 9(b) to a 13×13 matrix, which is shown by its submatrices as follows:

$$YA^T = \begin{bmatrix} 1 & 0 & 0 & 0 \\ -s\mathrm{C0} & 0 & 0 & 0 \\ -1 & 1 & 0 & 0 \\ 0 & 1 & 0 & -1 \\ 0 & 0 & 0 & -1 \\ 0 & 0 & 0 & -s\left(\frac{\mathrm{C}_{\pi1}+\mathrm{C}_{\pi2}}{2}\right) \\ 0 & -1 & 1 & 0 \\ 0 & 0 & -s\mathrm{C0} & 0 \\ 0 & 0 & -1 & 0 \end{bmatrix} \quad W = \begin{bmatrix} 0 \\ 0 \\ 0 \\ 1 \\ 0 \\ 0 \\ 0 \\ 0 \\ 0 \end{bmatrix}$$

$$A = \begin{bmatrix} -1 & 1 & 1 & 0 & 0 & 0 & 0 & 0 & 0 \\ 0 & 0 & -1 & 1 & 0 & 0 & 1 & 0 & 0 \\ 0 & 0 & 0 & 0 & 0 & 0 & -1 & 1 & 1 \\ 0 & 0 & 0 & -1 & 1 & 1 & 0 & 0 & 0 \end{bmatrix}$$

$$Z = \begin{bmatrix} s\mathrm{L0} & 0 & 0 & 0 & 0 & 0 & 0 & 0 & 0 \\ 0 & 1 & 0 & 0 & 0 & 0 & 0 & 0 & 0 \\ 0 & 0 & s\mathrm{L}_{\pi1} & 0 & 0 & 0 & 0 & 0 & 0 \\ 0 & 0 & 0 & 0 & 0 & 0 & 0 & 0 & 0 \\ 0 & 0 & 0 & 0 & \mathrm{Rt} & 0 & 0 & 0 & 0 \\ 0 & 0 & 0 & 0 & 0 & 1 & 0 & 0 & 0 \\ 0 & 0 & 0 & 0 & 0 & 0 & s\mathrm{L}_{\pi2} & 0 & 0 \\ 0 & 0 & 0 & 0 & 0 & 0 & 0 & 1 & 0 \\ 0 & 0 & 0 & 0 & 0 & 0 & 0 & 0 & s\mathrm{L0} \end{bmatrix}. \tag{5}$$

Solving this set of equations for V and I provides complex nodal voltages and branch currents dependent on the complex frequency s. Unlike the Simulink model-based approach that extracts RFs from the waveform of V_p simulated in the time domain, the Tableau formula focuses on the frequency-domain calculation directly and is expected to provide a more efficient solution to the RF estimation. However, the Tableau formula can be applied to the LPL model only, which must have sufficient π-sections to represent the frequency range required.

III. Assessment of Modelling Approaches

In this section, the RFs of the simplified DC traction power supply system will be estimated by the Simulink model and the modified Tableau formula based on a DPL model and/or LPL models with different numbers of π-sections, respectively. The consistency of the Simulink- and Tableau-based approaches and that of different line models are investigated.

A. Consistency of Simulink Model and Tableau Formula

Since the Tableau formula can be applied to a network with a finite number of states only, the consistency of the

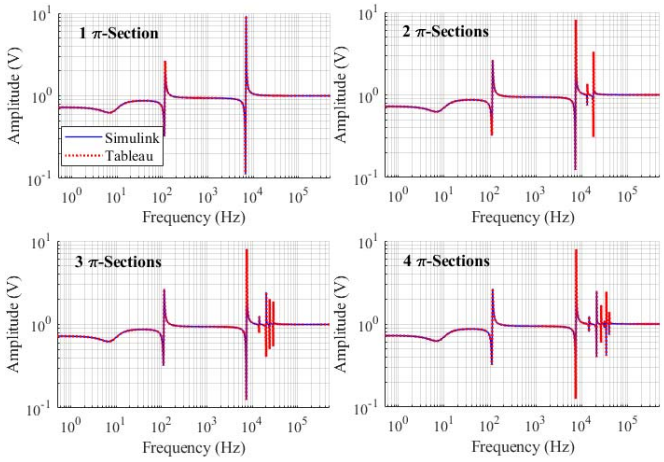

Fig. 10. Spectrums of V_p simulated by the Simulink model and Tableau formula using 1-4 π-sections to represent 9- and 11-km OHL segments, respectively.

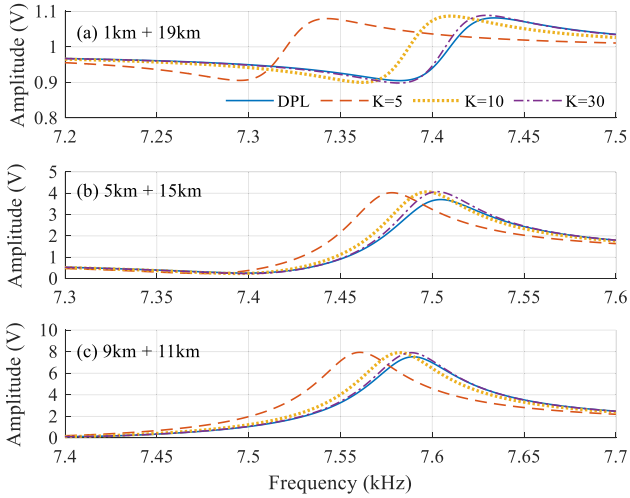

Fig. 11. Spectrums of V_p around the first RF related to the 20-km line simulated by DPL and LPL models with different numbers (K) of π-sections for three particular locomotive positions. (a) 1 + 19 km. (b) 5 + 15 km. (c) 9 + 11 km.

Simulink- and Tableau-based approaches is assessed here by use of the LPL-based simplified railway system model (see Fig. 9). When the locomotive splits the 20-km OHL into two segments with lengths of 9 and 11 km, spectrums of V_p estimated by the two approaches using $K\pi$-sections are compared in Fig. 10. As expected, the two approaches are in high agreement. The relative differences between the RF levels (Hz) estimated by the two approaches are found to increase with the RF level, from smaller than 0.02% for the first OHL-related RFs of around 7.5 kHz to about 0.5% for the RFs of around 40 kHz. Since the first OHL-related RF is to be adopted for the arc positioning, the two approaches on the basis of LPL models are considered to be consistent with a difference smaller than 1.5 Hz for the first RF related to the 20-km OHL. In all scenarios, the amplitude increases to a relative maximum at 113 Hz, which is close to the RF of the *LC* filter at the output stage of each TSS. The number of the RFs exceeding 7 kHz, which are related to 9- and 11-km line segments, equals $(2K-1)$, which is the same as the number of the equivalent capacitors in the OHL circuit, as noted in Section II-C.

B. Consistency of DPL and LPL Models

Though the modified Tableau formula directly focusing on the frequency-domain calculation uses less computation time for the RF estimation compared to the Simulink approach, it relies on LPL models and would need a sufficient number of π-sections to improve the accuracy of LPL models in transient response simulation. To determine the value of K that would be required in LPL models to produce the same RFs as DPL models, the V_p frequency spectrums estimated based on DPL and LPL models with different $K\pi$-sections are compared. Fig. 11 shows the V_p spectrums around the first OHL-related RFs simulated by the Simulink model based on DPL and LPL models with 5, 10, and 30 π-sections for three particular locomotive positions, respectively. The consistency of the DPL and LPL models in the simulation of the first OHL-related RFs is largely improved by increasing K from 5 to 10. However, a further increase to $K = 30$ gives a relatively slight improvement in their consistency at the cost of the network complexity and computation burden. It is found that there always exists a deviation between the first RFs simulated by the DPL and LPL models even if more π-sections are employed to represent each OHL segment due to the lumped parameter approximation [38]. Therefore, the investigation into the characteristics of the OHL-related RFs must be implemented by using DPL models in conjunction with the Simulink model, so as to improve the accuracy of the first OHL-related RF simulation.

It is noted that, in Fig. 11, there is a variation in the error of the RF as computed using five π-sections compared to the DPL. In Fig. 11(a), the deviation of the RF of $K = 5$ to the RF of the DPL is around 90 Hz. In Fig. 11(b) and (c), the same deviation is about 25 Hz. This variation is due to the fact that the same number of π-sections is applied to the 19-km segment of the line [see Fig. 11(a)] and the 11-km segment of the line [see Fig. 11(c)]. This leads to a different effective resolution of π-sections per kilometre of the track and leads to the error being dependent on the locomotive position. Appropriate modelling of the π-sections (e.g., a consistent number of π-sections per kilometre of the track) can eliminate this effect.

IV. RF Curve for Arc Location Estimation

Using the Simulink-based approach integrated with the DPL model, the influences of locomotive positions, total line lengths, and the V–I monitoring architecture on the RFs are investigated in this section. An RF curve linking the OHL-related RF with the arc position is then created and tentatively used to estimate the presumed arc location along the 20-km line.

A. Impacts of Locomotive Position and Line Length on RFs

The train moving along a line between two TSSs changes the location at which the line is split and, thus, the network

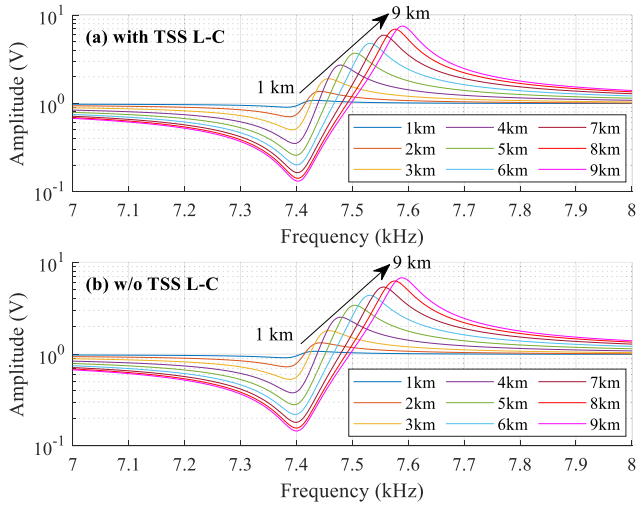

Fig. 12. Frequency spectrums of V_p around the first OHL-related resonance simulated for different TSS-locomotive distances (km) along a 20-km line when *LC* filters at TSS are (a) kept (with TSS *LC*) or (b) removed (without TSS *LC*).

topology and associated RFs. The influences of locomotive positions on resonances and antiresonances of the circuit impedance were explored in [35], [44], and [45] where the equivalent pantograph impedance Z_p made of the left and right OHL segments was formulated by

$$Z_p = Z_c \cdot \frac{\tanh(\gamma \cdot D_{\mathrm{TSS1}}) \cdot \tanh(\gamma \cdot D_{\mathrm{TSS2}})}{\tanh(\gamma \cdot D_{\mathrm{TSS1}}) + \tanh(\gamma \cdot D_{\mathrm{TSS2}})} \tag{6}$$

where D_{TSS1} and D_{TSS2} are distances (km) from the locomotive to the two TSSs and the terms Z_c and γ denote the characteristic impedance (Ω) and propagation constant (km^{-1}) of the line, respectively. The RFs (Hz) of Z_p have been found to be approximately independent of the locomotive position, while the antiresonant frequencies will vary with the locomotive position [44], [45]. Since this article deals with the signals of V_p across the train input, which is inversely associated with Z_p, the OHL-related resonance in the V_p frequency spectrum will correspond to the antiresonance of Z_p and, thus, vary with the train movement. The first resonance related to the 20-km line in the V_p spectrum changing with the locomotive location is shown in Fig. 12(a) where its amplitude and location both increase with the TSS-locomotive distance. Furthermore, the OHL-related antiresonance in the V_p spectrum is approximately fixed for different locomotive locations. Similar findings can be also obtained when the *LC* filter at each TSS output is removed, as shown in Fig. 12(b), meaning that the existence of *LC* filters at TSSs alongside the OHL circuit would not affect the variation of the OHL-related resonance with the TSS-locomotive distance.

Fig. 13 shows levels (kHz) and amplitudes (V) of OHL-related RFs estimated by the DPL-based Simulink model for different locomotive positions along the first half of the 20-km line. Though the OHL simulated by a DPL model has an infinite number of RFs, its first–fourth RFs are presented here. When the locomotive is near a particular TSS, the amplitudes of OHL-related RFs are dampened by the influence of the *LC* filter at the TSS output [46]. When heading to the middle

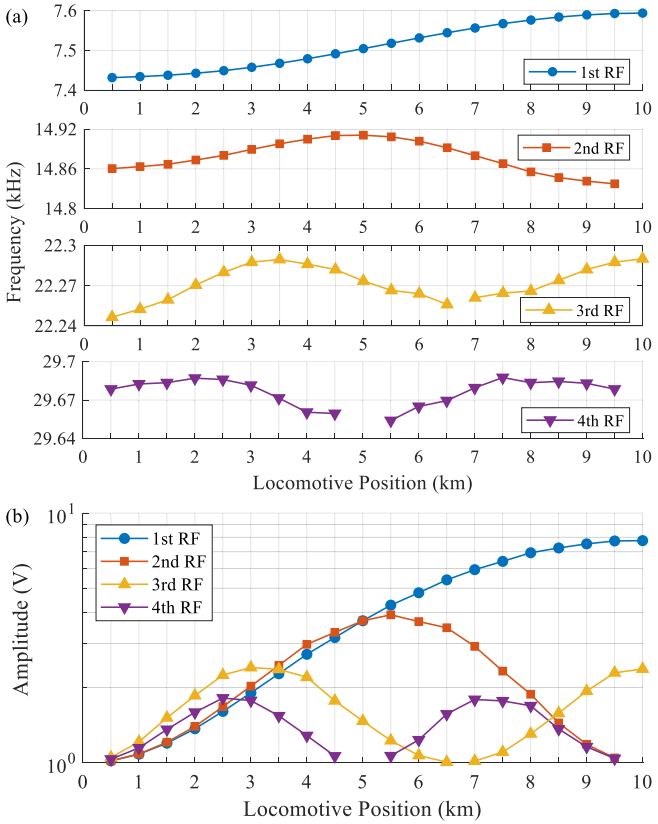

Fig. 13. (a) Levels (kHz) and (b) amplitudes (V) of the first–fourth RFs related to a 20-km OHL split at different locomotive positions (km away from a particular TSS).

of the line, only the first RF monotonically increases to its maximum in both level and amplitude, while the other RFs present periodic changes. These periodic changes arise from the symmetry of the segmented line. When the locomotive is exactly in the middle of the line, it forms two identical segments that are in parallel, thus eliminating half of the RFs, specifically all the even RFs. This can be seen in Fig. 13 where the second and fourth RFs disappear at 10 km. Similarly, the third RF cannot be detected at 6.67 km or 1/3 of the total line length, while the fourth RF disappears at all multiples of 1/4 of the total line length, i.e., at 5, 10, and 15 km (the last is not shown). Fig. 14 shows the V_p spectrum around the fourth RF for the locomotive positions between 3.5 and 6.5 km where the resonance disappears at 5 km. Compared with higher order RFs, the first RF that can be always deduced from spectrums and monotonically varies along each half of the line is expected to be a suitable indicator for the locomotive location.

In addition to the locomotive location, the total length of the OHL affects its related RFs. Fig. 15 shows the plots of the first RFs related to 30- and 40-km OHLs split by the locomotive at different positions along the first half of the OHL. With the line length increasing from 20 to 30 or 40 km, the range of the first RFs is shown to decrease from 7.4–7.6 [see Fig. 13(a)] to 4.95–5.15 [see Fig. 15(a)] or 3.7–3.9 kHz [see Fig. 15(b)], respectively. Therefore, the bandwidth of the V–I monitoring device required to capture the first RFs from V_p measurements

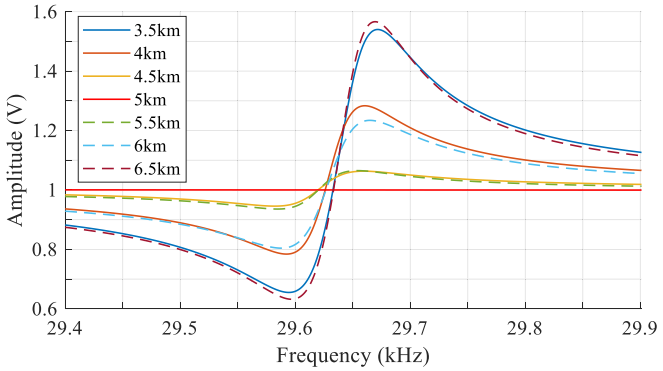

Fig. 14. V_p spectrums around the fourth RFs related to a 20-km OHL split by the locomotive that is 3.5–6.5 km away from a particular TSS.

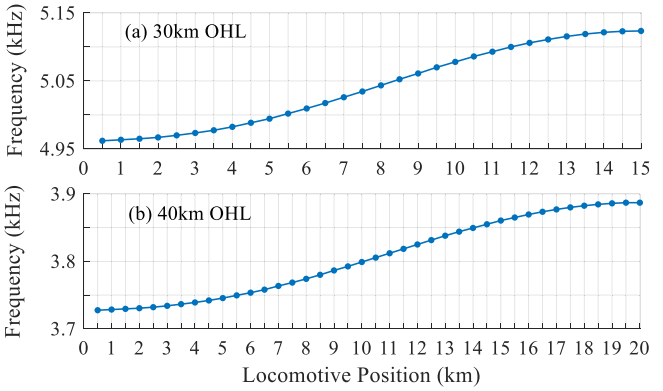

Fig. 15. Levels (kHz) of the first RFs related to 30- and 40-km lines split at different locomotive positions (km away from a particular TSS). (a) 30-km OHL. (b) 40-km OHL.

needs to increase for a reduced line length. This is because the amplitude of the first RF will be largely dampened if the first RF exceeds the bandwidth.

It is noted that the monotonic increase of the first RF (Hz) with the TSS-locomotive distance along each half of a line is only available in the scenario where the line is supplied by a TSS at each terminal. When the line is supported by a single TSS at either terminal, the first RF will monotonically decrease with the TSS-locomotive distance [47].

B. Impacts of V–I Monitoring Architecture on RFs

It should be noted that the aforementioned analysis of OHL-related RFs is conducted based on the V_p simulated at the input stage of the locomotive (see Fig. 7). In practice, an onboard V–I monitoring device must be used to measure V_p such that the monitoring architecture inclusive of a voltage divider and a DAS (see Fig. 3) may affect the estimated RF. In order to assess the impact of the monitoring architecture on RFs, a chirp signal is injected at the pantograph (i.e., the CVS) in the complete simulation model in Fig. 3. The V_p spectrum, including RFs, is estimated from the waveform of V_p as observed at the output of the V–I monitoring device. As was noted in Section IV-A, the DAS needs a bandwidth of at least the frequency of the first RF, here, 7.6 kHz for the

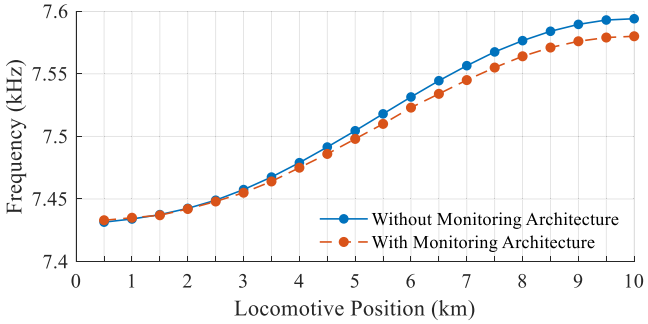

Fig. 16. First RFs (kHz) related to the 20-km line estimated for different locomotive positions (km away from a particular TSS) based on the V_p simulated at the monitoring device and those at the input stage of the train without connecting the sensor.

20-km OHL. The existing DAS represented by the 3.3-kHz *LC* filter in Fig. 3 would reduce the amplitude of the first RF, making it difficult to be detected in practice. An alternative voltage transducer [48] applicable for 3-kV DC measurements can provide up to 13-kHz bandwidth. In order to change the model of Fig. 3 to represent this new transducer, each component in the *LC* filter representing the DAS is adjusted to 25% of the original value in Table I. The resulting RF of the filter is about 13.2 kHz. Fig. 16 compares the first RFs related to the 20-km OHL determined from the V_p simulated at the monitoring device and those at the input stage of the locomotive without connecting the monitoring device. It shows that, in the main, the monitoring device does not affect the availability and monotonic characteristics of the estimated first RFs along each half of the line but slightly reduces their levels by around 10 Hz when the locomotive is close to the middle of the OHL. This is because the existence of the monitoring device increases the circuit impedance and, thus, reduces the levels of OHL-related RFs. When approaching a particular TSS, the differences between the estimated first RFs are gradually eliminated since the impedance increase becomes smaller relative to the circuit impedance without a monitoring device.

C. Use of RF Curve for Arc Location Estimation

The RF curve (see Fig. 16) that links the first OHL-related RF with the locomotive position taking into account the monitoring device is tentatively used here to estimate the location of a detected pantograph arc event along the first half of the 20-km line. Three arc events with the voltage profile fine-tuned, as shown in Fig. 5(a), are presumed to occur at three particular positions, i.e., 1, 5, and 9 km away from the left TSS. The profile of the arc voltage V_{arc} is taken into the CVS in the complete railway power system model (see Fig. 3) to simulate the waveform of the resulting V_p at the monitoring device for each pantograph arc location, respectively, as shown in Fig. 17. The deviations among the three V_p waveforms are caused by the varying arc position, which changes the network topology and RFs related to the OHL.

In order to detect the first OHL-related RF that implies the arc location, the three V_p waveforms simulated in the

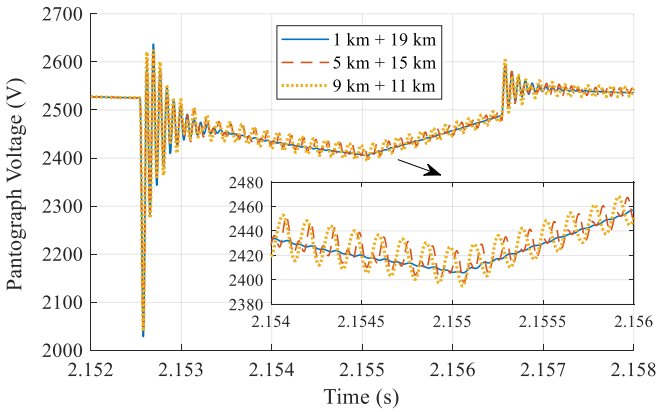

Fig. 17. Time series of V_p simulated at the V–I monitoring device based on the fine-tuned voltage profile of a pantograph arc event occurring at three particular positions along the first half of the 20-km OHL.

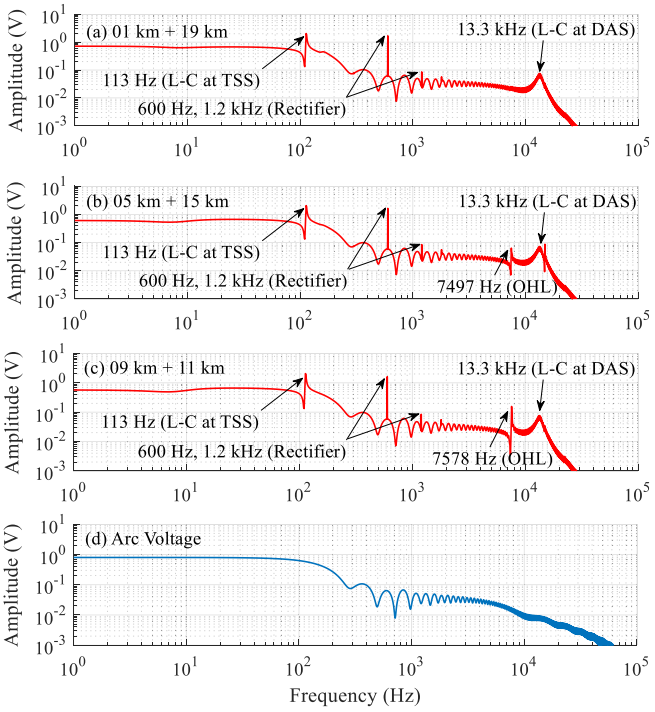

Fig. 18. Spectrums of V_p simulated at the monitoring device for the presumed arc events occurring at (a) 1, (b) 5, and (c) 9 km away from the left TSS and (d) spectrum of the fine-tuned arc voltage profile. (a) 1 + 19 km. (b) 5 + 15 km. (c) 9 + 11 km.

time domain are converted into the frequency domain by the FFT, as shown in Fig. 18(a)–(c). It is noted that, unlike the previous V_p spectrums that are calibrated based on FCs of a chirp signal, these V_p spectrums reflect the FCs of V_{arc} [see Fig. 18(d)] since the exact V_{arc} profile is not available to calibrate the V_p spectrum in practice. Each V_p spectrum shows resonances at around 113 Hz and 13.3 kHz, which are associated with the filter placed at the TSS output and the filter representing the DAS, respectively. In addition, the use of 12-pulse rectifiers (see Fig. 3) results in harmonics at integer multiples of the 12th harmonic of the nominal 50 Hz, i.e., 600 Hz [49].

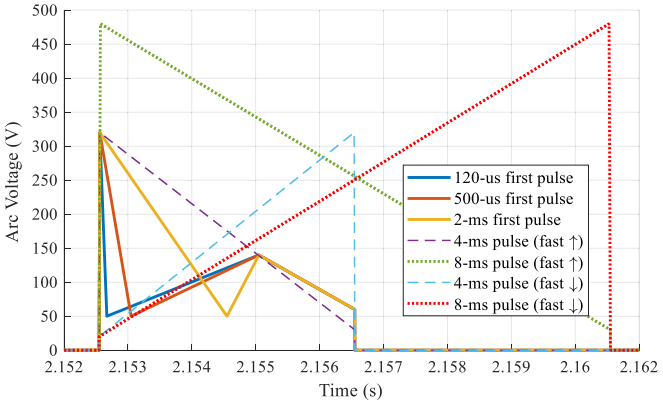

Fig. 19. Presumed pantograph arc voltage profiles with varying pulse durations and amplitudes for the test of the arc positioning method.

Since the amplitude of the first RF related to the OHL split into 1- and 19-km segments is quite small [see Fig. 13(b)], it is difficult to determine the resonance related to the OHL in Fig. 18(a) where the V_p spectrum around the first OHL-related RF mainly depends on the FC of the arc voltage (FC_{arc}). With the arc position being closer to the middle of the line, the first OHL-related RF has a higher amplitude such that the OHL-related resonance can be detected, i.e., around 7497 and 7578 Hz for the arc events occurring at 5 and 9 km from the left TSS, as shown in Fig. 18(b) and (c), respectively. According to the OHL-related RF curve (see Fig. 16), which is formed on the basis of the calibrated V_p spectrums, the detected resonances indicate that the arc events may occur at around 4.95 and 9.33 km from the left TSS, with errors of 0.05 and 0.33 km, respectively (i.e., differences between the presumed and estimated locations).

The use of the RF curve for arc positioning is also examined for other pantograph arc events that are presumed to occur along the first half of the line at different positions greater than 2.5 km from the left TSS (below which the OHL-related resonances are difficult to be detected in the V_p spectrums). In addition to the fine-tuned V_{arc} profile in Fig. 5(a) where the duration of the first pulse is 120 μs, different V_{arc} profiles with a longer first pulse of 500 μs or 2 ms or a single pulse of 4 or 8 ms, as shown in Fig. 19, are used here to test the arc positioning method. The differences between the presumed positions and their respective estimates are plotted in Fig. 20, where the V_{arc} profiles tested here with varying amplitudes and pulse durations are shown to have similar arc location estimation errors. Relatively smaller errors (e.g., within $\pm$0.2 km) are observed for the presumed arc locations between 4 and 8 km. This is because when the locomotive locates at around 4–8 km, the deviation (Hz) of the FC_{arc} affected RF from the calibration-based RF leads to a relatively smaller change in the locomotive position, as shown in the RF curve, which has a higher gradient for the TSS-locomotive distances of about 4–8 km in Fig. 16.

V. Discussion

Considering that the wires making up OHLs in railway traction systems are generally around 1.5-km long [50], the arc

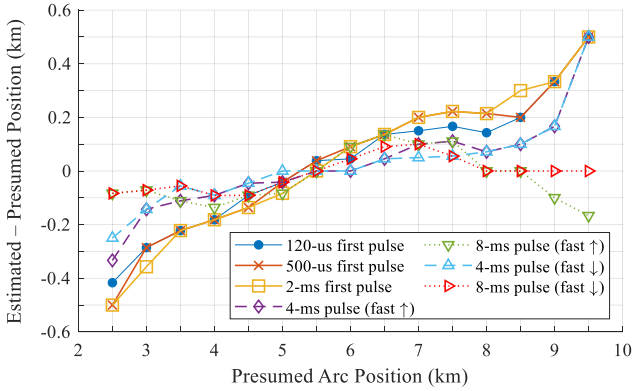

Fig. 20. Deviations (km) between the estimated and presumed arc locations that are 2.5–9.5 km away from the left TSS.

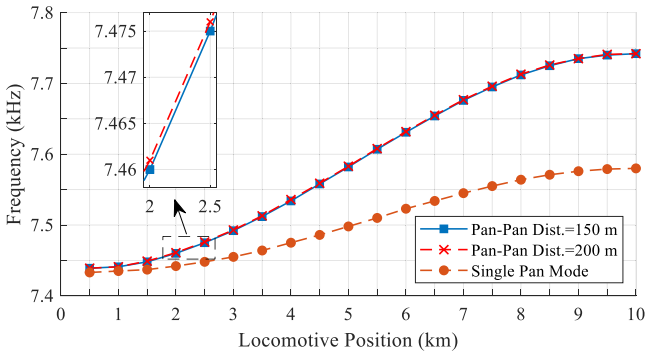

Fig. 21. First RFs related to the 20-km line observed at the left pantograph in the double-pantograph mode for different locomotive positions (i.e., distances from left pantograph to left TSS) when two pantographs are 150 or 200 m apart.

position estimate with an error of up to 0.4 km in most cases is expected to correctly indicate the wire where the arc has occurred in this work. If repeated arcs are detected approximately at the same position, the suspected OHL section will need an inspection. However, it should be pointed out that further work needs to deal with the limitations that the arc positioning method has in the application: 1) it could be difficult to detect the RF when an arc event is very close to a TSS due to the dampening effect of the filter at the TSS output; 2) the method infers arc positions along either half of a line that is supplied by two TSSs at both terminals, without indicating which half may be in question; and 3) an arc position cannot be determined if the FC_{arc} affected RF is greater than the maximum level of the RF curve (e.g., the RF of 7582 Hz estimated for an arc at the middle of the 20-km line exceeding the maximum of 7580 Hz in the RF curve disables the arc positioning method).

The pantograph arc positioning method developed here can be extended to double-pantograph current collection modes that are normally adopted by multiple-unit trains [51]. To generate an RF curve for the double-pantograph operation, the complete simulation model in Fig. 3 needs to be modified by placing an additional set of train components in parallel with the existing set and adding an additional OHL segment between the two train sets. Given the distance between pantographs (or the additional OHL segment length) being 150 or 200 m, the first OHL-related RFs observed at the left pantograph are estimated for different locomotive positions (i.e., distances from left TSS to left pantograph), as shown in Fig. 21. (The OHL-related RFs at the right pantograph can be inferred from Fig. 21.) The first RFs varying between 7.44 and 7.74 kHz in the double-pantograph mode have a wider range than those when a single pantograph is simulated. In addition, a 50-m increase of the distance between pantographs results in a slight growth of the first OHL-related RFs. When pantograph arcing is determined at a particular pantograph, the RF curve produced for double-pantograph modes in Fig. 21 can be compared with the RFs captured from onboard measurements to estimate the pantograph arc location along the OHL.

In order to capture the first OHL-related RFs from V_p signals, the bandwidth of onboard V–I monitoring devices should be several times greater than the maximum level of the first RFs so as to avoid the amplitude of the first RF being largely dampened if the first RF exceeds the bandwidth. This requires determining the range (kHz) of the first RFs in advance based on the line length and available values of circuital components, including line impedance parameters. In addition, the sampling frequency of V–I monitoring devices must be greater than twice the maximum level of the first OHL-related RF so that the frequency range of the FFT spectrum can cover the first RFs according to the Nyquist criterion [52]. For example, the 20-km line modelled here would require a sampling frequency of at least 16 kHz. The frequency resolution of the FFT spectrum is determined by the ratio of the sampling frequency to the number of V_p measurement points [52] or the reciprocal of the length of V_p measurements in the time domain. Though a higher resolution can be achieved by applying the FFT to a longer measurement window size, the TSS-locomotive distance would vary so much in a long time period that the accuracy of the first RF associated with the arc location may be degraded. Considering a tradeoff between the frequency resolution and the train travel distance, a 1-Hz resolution (i.e., applying FFT to a 1-s window of V_p measurements) is expected to be a reasonable option due to its performance assessed in Fig. 20 and that a 250-km/h train ETR600 [30] traveling less than 70 m over 1 s is found to incur the first RF deviation within 1 Hz.

The RF curves embedded within the arc positioning method have been generated here based on known OHL impedance parameters, which, however, maybe not with good precisions in practice. A sensitivity analysis is conducted here to investigate impacts of the line impedance parameter uncertainty on RFs. Fig. 22 compares the first OHL-related RFs evaluated for the TSS-locomotive distance of 1, 5, or 10 km based on different combinations of line inductance and capacitance parameters that are assumed to vary within 10% of their respective values in Table I. A 2% underestimation in the inductance or capacitance is shown to overestimate the first RFs by about 60–70 Hz in this case, which would affect the

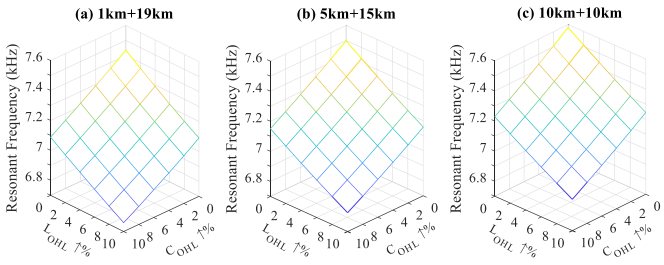

Fig. 22. First OHL-related RFs simulated for TSS-locomotive distances of (a) 1, (b) 5, and (c) 10 km given the line inductance L_{OHL} and/or capacitance C_{OHL} increasing by 0%–10%. (a) 1 + 19 km. (b) 5 + 15 km. (c) 10 + 10 km.

arc positioning method performance. Therefore, it is necessary to validate the impedance parameters of OHL sections based on field measurement campaigns [53]–[55] in order to improve the accuracy of the generated RF curve. In addition, the Simulink DPL blocks [33] used here do not accurately represent the frequency dependence of line impedance parameters (e.g., skin effects in conductors). The frequency-dependent DPL blocks [56] could be suitable substitutes to perform more accurate simulations for a wide frequency range (typically from DC to 100 kHz or more). Furthermore, considering that the validated and frequency-dependent line impedance parameters may be still subject to uncertainties, their possible errors can be translated into the uncertainty of the RF curve by some statistical models (e.g., the Monte Carlo simulation [57]), permitting a probabilistic estimation of the pantograph arc position. This would require embedding multiple RF curves evaluated based on various combinations of line impedance parameters within the arc positioning method.

VI. Conclusion and Future Work

This article has proposed a V–I measurement-based method to determine the pantograph arc location along an OHL supported by two TSSs in a DC railway traction power supply system. The proposed method relies on an RF curve that links the OHL-related RF with the pantograph arc location at which the line is split. The line simulated by a distributed parameter model has an infinite number of RFs, from which the first RF is selected to produce the RF curve. This is because the first RF monotonically increases with the TSS-locomotive distance along each half of the line, while the higher order RFs present periodic changes. The monotonic characteristics of the first OHL-related RFs have been validated for 20-, 30-, and 40-km OHLs, with their levels (Hz) decreasing with the total length of the line.

The proposed arc positioning method has been tested on the waveforms of pantograph voltage V_p simulated at the onboard monitoring device based on the fine-tuned arc voltage profiles that are presumed to occur at different positions along the first half of a 20-km line. Most of the presumed arc positions have been estimated with errors smaller than 0.4 km; for pantograph arc events occurring at around 4–8 km from the TSS where the RF curve has a higher gradient, the position estimation errors should be within 0.2 km. When an arc event is very close to a TSS (e.g., a TSS-locomotive distance smaller than 2.5 km in this study), the amplitudes of OHL-related RFs are largely dampened by the filter at the TSS output, making it difficult to detect the OHL-related resonance from the V_p spectrum.

Building on this work, the proposed arc positioning method should be developed further to determine the half of the line in question and deal with the exceedance of an RF estimate over the range of an RF curve. Furthermore, the method will be enhanced to simulate the frequency-dependent impedance parameters and model the propagation of OHL impedance uncertainties to the uncertainty of the RF curve. In addition, the arc positioning method will require to be evaluated on more arc voltage profiles produced by pantograph arcing models [58], [59] that could better describe transient dynamics of arc voltage, as well as on field measurements of V_p available onboard trains. This requires the monitoring device to have a bandwidth several times greater than the maximum level of the first RFs related to the OHL of interest so as not to attenuate amplitudes of the first RFs. The field data in the measured pantograph arc events will be explored to validate the findings in this article regarding the change of the first RF with pantograph arc location along the OHL and also determine the accuracy of the captured RFs. It will also be necessary to examine the benefit of adopting a higher sampling rate monitoring system, which could increase the RF detection accuracy or even eliminate the need for a low-pass filter at the DAS, without having to accurately characterise the filter response to correct RF curves.

Acknowledgment

The research was developed under the 16ENG04 MyRailS Project. Support for the work described in this article is gratefully acknowledged by the partners of the MyRailS Project.

References

[1] *Electrification of the Transport System, Studies and Reports*, Directorate Gen. Res. Innov., Eur. Commission, Brussels, Belgium, 2017.
[2] *Moving Towards Sustainable Mobility—A Strategy for 2030 and Beyond for the European Railway Section*, Int. Union Railways, Paris, France, 2012.
[3] F. Fan and B. G. Stewart, "Power flow simulation of DC railway power supply systems with regenerative braking," in *Proc. IEEE 20th Medit. Electrotech. Conf. (MELECON)*, Palermo, Italy, Jun. 2020, pp. 87–92.
[4] R. D. White, "DC electrification supply system design," in *Proc. 3rd IET Prof. Develop. Course Railway Electrific. Infrastruct. Syst.*, London, U.K., Jun. 2007, pp. 1–29.
[5] F. Fan, Y. Li, S. Ziani, and B. G. Stewart, "Reversible substation modelling with regenerative braking in DC traction power supply systems," in *Proc. IEEE Texas Power Energy Conf. (TPEC)*, Austin, TX, USA, Feb. 2021, pp. 1–6.
[6] J. Wu, *Pantograph and Contact Line System*, 1st ed. London, U.K.: Academic, 2018.
[7] O. Bruno, A. Landi, M. Papi, and L. Sani, "Phototube sensor for monitoring the quality of current collection on overhead electrified railways," *Proc. Inst. Mech. Eng. F, J. Rail Rapid Transit*, vol. 215, no. 3, pp. 231–241, May 2001.
[8] S. Midya, D. Bormann, T. Schutte, and R. Thottappillil, "Pantograph arcing in electrified railways—Mechanism and influence of various parameters—Part I: With DC traction power supply," *IEEE Trans. Power Del.*, vol. 24, no. 4, pp. 1931–1939, Oct. 2009.
[9] G. Wu, G. Gao, W. Wei, and Z. Yang, "Friction and wear of pantograph and catenary," in *The Electrical Contact of the Pantograph-Catenary System: Theory and Application*, 1st ed. Singapore: Springer, 2019, ch. 3, pp. 71–107.

[10] Y. Song, P. Antunes, J. Pombo, and Z. Liu, "A methodology to study high-speed pantograph-catenary interaction with realistic contact wire irregularities," *Mechanism Mach. Theory*, vol. 152, Oct. 2020, Art. no. 103940.

[11] Y. Song, Z. Liu, A. Rønnquist, P. Nåvik, and Z. Liu, "Contact wire irregularity stochastics and effect on high-speed railway pantograph–catenary interactions," *IEEE Trans. Instrum. Meas.*, vol. 69, no. 10, pp. 8196–8206, Oct. 2020.

[12] H. Wang, A. Núñez, Z. Liu, Y. Song, F. Duan, and R. Dollevoet, "Analysis of the evolvement of contact wire wear irregularity in railway catenary based on historical data," *Vehicle Syst. Dyn.*, vol. 56, no. 8, pp. 1207–1232, Aug. 2018.

[13] *Railway Applications—Current Collection Systems—Technical Criteria for the Interaction Between Pantograph and Overhead Line*, Standard EN 50367, British Standards Inst., London, U.K., Jan. 2012.

[14] Y. Song, A. Ronnquist, and P. Navik, "Assessment of the high-frequency response in railway pantograph-catenary interaction based on numerical simulation," *IEEE Trans. Veh. Technol.*, vol. 69, no. 10, pp. 10596–10605, Oct. 2020.

[15] *Railway Applications—Fixed Installations—Electric Traction Overhead Contact Lines*, Standard EN 50119, British Standards Inst., London, U.K., Apr. 2020.

[16] I. Aydin, M. Karakose, and E. Akin, "A new contactless fault diagnosis approach for pantograph-catenary system using pattern recognition and image processing methods," *Adv. Elect. Comput. Eng.*, vol. 14, no. 3, pp. 79–88, Aug. 2014.

[17] S. Huang, L. Yu, F. Zhang, W. Zhu, and Q. Guo, "Cluster analysis based arc detection in pantograph-catenary system," *J. Adv. Transp.*, vol. 2018, May 2018, Art. no. 1329265.

[18] G. Karaduman, M. Karaköse, and E. Akin, "Deep learning based arc detection in pantograph-catenary systems," in *Proc. 10th Int. Conf. Electr. Electron. Eng.*, Bursa, Turkey, Dec. 2017, pp. 1–5.

[19] C. J. Cho and H. Ko, "Video-based dynamic stagger measurement of railway overhead power lines using rotation-invariant feature matching," *IEEE Trans. Intell. Transp. Syst.*, vol. 16, no. 3, pp. 1294–1304, Jun. 2015.

[20] A. Landi, L. Menconi, and L. Sani, "Hough transform and thermo-vision for monitoring pantograph-catenary system," *Proc. Inst. Mech. Eng. F, J. Rail Rapid Transit*, vol. 220, no. 4, pp. 435–447, Jul. 2006.

[21] O. Bruno, A. Landi, M. Papi, L. Sani, and A. G. Violi, "Pantograph-catenary monitoring: Correlation between break arcs and harmonics in the traction currents," in *Proc. World Conf. Railway Res.*, Koln, Germany, Oct. 2001, pp. 1–17.

[22] *Railway Applications—Current Collection Systems—Requirements for and Validation of Measurements of the Dynamic Interaction Between Pantograph and Overhead Contact Line*, Standard EN 50317, Brit. Standards Inst., London, U.K., 2012.

[23] G. Gao, X. Yan, Z. Yang, W. Wei, Y. Hu, and G. Wu, "Pantograph–Catenary arcing detection based on electromagnetic radiation," *IEEE Trans. Electromagn. Compat.*, vol. 61, no. 4, pp. 983–989, Aug. 2019.

[24] L. Ma, Y. Wen, K. Zhou, J. Zhang, D. Zhang, and Q. Shan, "Research on electromagnetic radiated disturbance of pantograph arc in high-speed railway," in *Proc. 5th IEEE Int. Symp. Microw., Antenna, Propag. EMC Technol. Wireless Commun.*, Chengdu, China, Oct. 2013, pp. 637–641.

[25] S. Barmada, A. Landi, M. Papi, and L. Sani, "Wavelet multiresolution analysis for monitoring the occurrence of arcing on overhead electrified railways," *Proc. Inst. Mech. Eng. F, J. Rail Rapid Transit*, vol. 217, no. 3, pp. 177–187, May 2003.

[26] Y. Seferi, S. M. Blair, C. Mester, and B. G. Stewart, "A novel arc detection method for DC railway systems," *Energies*, vol. 14, pp. 1–21, Jan. 2021, Paper 444.

[27] S. Barmada, M. Raugi, M. Tucci, and F. Romano, "Arc detection in pantograph-catenary systems by the use of support vector machines-based classification," *IET Electr. Syst. Transp.*, vol. 4, no. 2, pp. 45–52, Jun. 2014.

[28] I. Aydin, S. B. Celebi, S. Barmada, and M. Tucci, "Fuzzy integral-based multi-sensor fusion for arc detection in the pantograph-catenary system," *Proc. Inst. Mech. Eng. F, J. Rail Rapid Transit*, vol. 232, no. 1, pp. 159–170, Jan. 2018.

[29] S. Barmada, M. Tucci, M. Menci, and F. Romano, "Clustering techniques applied to a high-speed train pantograph–catenary subsystem for electric arc detection and classification," *Proc. Inst. Mech. Eng. F, J. Rail Rapid Transit*, vol. 230, no. 1, pp. 85–96, Jan. 2016.

[30] G. Crotti *et al.*, "Pantograph-to-OHL arc: Conducted effects in DC railway supply system," *IEEE Trans. Instrum. Meas.*, vol. 68, no. 10, pp. 3861–3870, Oct. 2019.

[31] *MATLAB Release*, MathWorks, Natick, MA, USA, 2019.

[32] M. Popescu and A. Bitoleanu, "A review of the energy efficiency improvement in DC railway systems," *Energies*, vol. 12, Mar. 2019, Art. no. 1092.

[33] The MathWorks. (2020). *Distributed Parameter Line*. [Online]. Available: https://www.mathworks.com/help/physmod/sps/powersys/ref/distributedparameterline.html

[34] G. Bucca and A. Collina, "A procedure for the wear prediction of collector strip and contact wire in pantograph–catenary system," *Wear*, vol. 266, nos. 1–2, pp. 46–59, Jan. 2009.

[35] A. Mariscotti and D. Giordano, "Experimental characterization of pantograph arcs and transient conducted phenomena in DC railways," *ACTA IMEKO*, vol. 9, no. 2, pp. 10–17, Jun. 2020.

[36] The MathWorks. (2020). *Chirp Signal*. [Online]. Available: https://www.mathworks.com/help/simulink/slref/chirpsignal.html

[37] *Fourier Transforms and the Fast Fourier Transform (FFT) Algorithm*, Carnegie Mellon Univ., Pittsburgh, PA, USA, 1998, p. 15463.

[38] M. S. M. M. Koksal, "Remark on the lumped parameter modeling of transmission lines," *Electr. Mach. Power Syst.*, vol. 28, no. 6, pp. 565–575, Jun. 2000.

[39] I. M. Abdulaziz, "Mathematical modelling and computer simulations of induced voltage calculations in AC electric traction," Ph.D. dissertation, School Eng. Built Environ., Napier Univ., Edinburgh, U.K., 2003.

[40] N.R. Chaudhuri, B. Chaudhuri, R. Majumder, and A. Yazdani, *Multi-Terminal Direct-Current Grids, Modeling, Analysis, and Control*. Hoboken, NJ, USA: Wiley, 2014, pp. 87–89.

[41] J. Vlach, "Tableau and modified nodal formulation," in *The Circuits Filters Handbook*, 2nd ed. Boca Raton, FL, USA: CRC Press, 2003, ch. 22.

[42] The MathWorks. (2020). *PI Section Line*. [Online]. Available: https://www.mathworks.com/help/physmod/sps/powersys/ref/pisectionline.html

[43] J. E. Rayas-Sánchez, *The Modified Nodal Analysis (MNA) Method*. Tlaquepaque, Mexico: Univ. Jesuita de Guadalajara, 2020.

[44] A. Mariscotti and P. Pozzobon, "Synthesis of line impedance expressions for railway traction systems," *IEEE Trans. Veh. Technol.*, vol. 52, no. 2, pp. 420–430, Mar. 2003.

[45] A. Mariscotti and D. Giordano, "Electrical characteristics of pantograph arcs in DC railways: Infrastructure influence," in *Proc. 23rd IMEKO Int. Symp. Electr. Electron. Meas. Promote Ind.*, Xi'an, China, Sep. 2019, pp. 155–159.

[46] P. Ferravi, A. Maviscotti, and P. Pozzobon, "Reference curves of the pantograph impedance in DC railway systems," in *Proc. IEEE Int. Symp. Circuits Syst. Emerg. Technol.*, Geneva, Switzerland, May 2000, pp. 555–558.

[47] R. J. Hill, M. Fracchia, P. Pozzobon, and G. Sciutto, "A frequency domain model for 3 kV DC traction DC-side resonance identification," *IEEE Trans. Power Syst.*, vol. 10, no. 3, pp. 1369–1375, Aug. 1995.

[48] *Catalog Sensors-A1: Current Sensors, Voltage Sensors and Voltage Detectors*, Petercem, Frontonas, France, 2018. [Online]. Available: http://www.petercem.com/wp-content/uploads/2018/02/catalog-Sensors-A1_GB-BD.pdf

[49] R. Visintini, "Rectifiers," in *CAS CERN Accelerator School Specialized Course on Power Converters*. Geneva, Switzerland: CERN, 2006, pp. 133–183. [Online]. Available: https://cds.cern.ch/record/987551/files/p133.pdf

[50] F. Nyberg, R. Pollard, J. Mason, R. Thorne, A. Seek, and R. Payne, "Network rail: A guidance to overhead electrification," Alan Baxter Associate LLP, London, U.K., Tech. Rep. 132787-ALB-GUN-EOH-000001, 2015.

[51] X. Zhang and X. Chen, "Dynamic characteristic analysis of double-pantograph-catenary system of long marshalling EMU," in *Proc. IEEE 5th Inf. Technol. Mechatronics Eng. Conf. (ITOEC)*, Jun. 2020, pp. 264–269.

[52] M. Cerna and A. F. Harvey, "The fundamentals of FFT-based signal analysis and measurement," Nat. Instrum. Corp., Austin, TX, USA, Appl. Notes. 041, Jul. 2000.

[53] S. Brillante, G. D'Addio, P. Ferrari, A. Mariscotti, and P. Pozzobon, "Validation of the analytical model of an electric railway traction line," in *Proc. Int. Conf. Metrol.*, Jerusalem, Israel, May 2002, pp. 355–360.

[54] S. Brillante, G. D'Addio, P. Ferrari, A. Mariscotti, and P. Pozzobon, "Measurement techniques for validating the calculation methods of electric railway traction line parameters," in *Proc. Int. Conf. Metrol.*, Jerusalem, Israel, May 2002, pp. 154–161.

[55] J. C. García *et al.*, "Characterization of railway line impedance based only on short-circuit measurements," *Int. J. Circuit Theory Appl.*, vol. 43, no. 8, pp. 984–994, Aug. 2015.

[56] The MathWorks. (2020). *Distributed Parameter Line (Frequency-Dependent)*. [Online]. Available: https://www.mathworks.com/help/physmod/sps/powersys/ref/distributedparameterslinefrequencydependent.html
[57] R. Y. Rubinstein and D. P. Kroese, *Simulation and the Monte Carlo Method*. Hoboken, NJ, USA: Wiley, 2007.
[58] Y. Wang, Z. Liu, F. Fan, and S. Gao, "Review of research development of pantograph-catenary arc model and electrical characteristics," *J. China Railway Soc.*, vol. 35, no. 8, pp. 35–43, Aug. 2013.
[59] G. Gao, T. Zhang, W. Wei, Y. Hu, G. Wu, and N. Zhou, "A pantograph arcing model for electrified railways with different speeds," *Proc. Inst. Mech. Eng., F, J. Rail Rapid Transit*, vol. 232, no. 6, pp. 1731–1740, Jul. 2018.

Fulin Fan received the B.Eng. and Ph.D. degrees in electronic and electrical engineering from North China Electric Power University, Baoding, China, and the University of Strathclyde, Glasgow, U.K., in 2012 and 2018, respectively.

From 2016 to 2018, he was a Research Assistant with the University of Strathclyde, where he has been a Research Associate since 2018. His research interests include electric traction system modelling, real-time thermal rating forecasting for overhead lines, and energy storage optimisation.

Andreas Wank received the Diploma degree in electrical engineering from the Technical University of Munich, Munich, Germany, in 2012.

From 2014 to 2019, he was a Transmission System Operator with TenneT TSO GmbH, Hannover, Germany. He is currently a Research Scientist with the National Physical Laboratory, Glasgow, U.K. His research interests include power system modelling and design, power quality, and impedance measurements.

Yljon Seferi (Graduate Student Member, IEEE) was born in Tirana, Albania, in October 1983. He received the Diploma degree in electrical engineering from the Polytechnic University of Tirana, Tirana, in 2007. He is currently pursuing the Ph.D. degree with the Department of Electronic and Electrical Engineering, Institute for Energy and Environment, University of Strathclyde, Glasgow, U.K.

His research interests include phasor measurement unit design, power quality, power and energy measurements, and electrical metrology.

Brian G. Stewart (Member, IEEE) received the B.Sc. (Hons.) and Ph.D. degrees from the University of Glasgow, Glasgow, U.K., in 1981 and 1985, respectively, and the B.D. degree (Hons.) from the University of Aberdeen, Aberdeen, U.K., in 1994.

He is currently a Professor with the Institute for Energy and Environment, University of Strathclyde, Glasgow. His research interests are focused on high-voltage engineering, electrical condition monitoring, insulation diagnostics, and communication systems.

Prof. Stewart is also a Chartered Engineer (CEng) and a member of the Institution of Engineering Technology (MIET). He is also the Vice-President Administration of the IEEE Dielectrics and Electrical Insulation Society.